epic-AN-AC-2026-02

Light Meson Form Factors from Deep Exclusive Meson Production in early EIC science configurations with the ePIC Detector

Principal Author List:

G. M. Huber[1] - huberg@uregina.ca
S.J.D. Kay[2] - stephen.kay@york.ac.uk
L. Preet[1] - love.preet@uregina.ca

[1]Department of Physics, University of Regina, Saskatchewan, S4S 0A2, Canada
[2]School of Physics, Engineering and Technology, University of York, YO10 5DD, United Kingdom

(March 24, 2026)

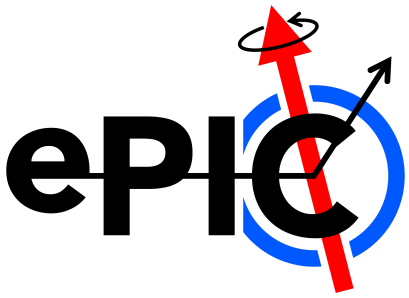

Abstract

The structure of light mesons offers a window into the mass generation mechanisms of QCD. In particular, the pion and kaon, the Nambu-Goldstone boson modes of QCD, are of particular interest. In this analysis note, prospects for studies of light meson form factors at the Electron-Ion Collider (EIC) by measuring **D**eep **E**xclusive **M**eson **P**roduction (DEMP) reactions with the ePIC detector system are presented. These studies focus on what will be achievable in the first five years of running at the EIC. Projections for the reach of pion form factors, F_π, in this "early science period" are presented, showcasing the potential to significantly extend the Q^2 reach of the world data set for F_π. The path forward for future studies is also presented.

Contents

1 Introduction

1.1 Scientific Motivation

Pions and kaons are among the most prominent strongly interacting particles next to the nucleon, since they are the Goldstone bosons of QCD. Thus, it is important to study their internal structure and how this reflects their Goldstone boson nature; a question particularly relevant for understanding the origin of mass generation in QCD.

The hard contribution to the π^+ form factor can be calculated exactly within the framework of pQCD, and at asymptotically high Q^2 it takes a particularly simple form, $F_\pi(Q^2) \overrightarrow{_{Q^2\to\infty}} 16\pi\alpha_s(Q^2) f_\pi^2/Q^2$ [1], where f_π is the π^+ decay constant. In general, the pion also contains soft contributions, which are expected to dominate at lower Q^2. The actual behavior of F_π as a function of Q^2, as QCD transitions smoothly from the non-perturbative (long-distance scale) confinement regime to the perturbative (short-distance scale) regime, is an important test of our understanding of QCD in bound hadron systems. Since QCD calculations cannot yet be performed rigorously in the confinement regime, experimental data from JLab play a vital role in validating the theoretical approaches employed. In particular, due to the charged pion's relatively simple quark-antiquark ($q\bar{q}$) valence structure and its experimental accessibility, the pion elastic form factor (F_π) offers our best hope of directly observing QCD's transition from color-confinement at long distance scales to asymptotic freedom at short distances. It is worth highlighting that in QCD the difference between the kaon and pion charge form factors is of the scale of 20% at $Q^2 \sim 5$ GeV^2 [2] and disappears at asymptotic Q^2 as $\ln(Q^2)$. Thus, the acquisition of experimental data for both form factors covering a wide Q^2 range should be a high priority.

1.2 Methodology

Current experimental information on the pion and kaon form factors is limited, particularly at large Q^2 [3]. Measurement of the π^+ electromagnetic form factor for $Q^2 > 0.3$ GeV^2 can be accomplished by the detection of the exclusive reaction $p(e, e'\pi^+)n$ at low $-t$. This is best described as quasi-elastic (t-channel) scattering of the electron from the virtual π^+ cloud of the proton, where $t = (p_p - p_n)^2$ is the Mandelstam momentum transfer to the target nucleon. Scattering from the π^+ cloud dominates the longitudi-

nal photon cross section ($d\sigma_L/dt$), when $|t| \ll m_p^2$. To reduce background contributions, one preferably separates the components of the cross section due to longitudinal (L) and transverse (T) virtual photons (and the LT, TT interference contributions), via a Rosenbluth separation,

$$2\pi\frac{d^2\sigma}{dtd\phi} = \epsilon\frac{d\sigma_{\rm L}}{dt} + \frac{d\sigma_{\rm T}}{dt} + \sqrt{2\epsilon(\epsilon+1)}\,\frac{d\sigma_{\rm LT}}{dt}\cos\phi + \epsilon\frac{d\sigma_{\rm TT}}{dt}\cos 2\phi, \qquad (1)$$

where $d\sigma_L/dt$ ($d\sigma_T/dt$) are due to longitudinal (transverse) photons, $d\sigma_{LT}/dt$, $d\sigma_{TT}/dt$ are interference cross-sections, $\epsilon = 2(1-y)/(1+(1-y)^2)$ is the virtual-photon polarization parameter, ϕ is the azimuthal angle between the electron scattering and hadron reaction planes, and $y = Q^2/(x(s_{tot} - m_N^2))$ is the fractional energy loss. For convenience, we will refer to the left side of this equation as σ_{uns}, *i.e.* the unseparated cross section.

A Rosenbluth separation involves the absolute subtraction of two measurements determined at high- and low-virtual photon polarization (ϵ_{Hi}, ϵ_{Lo}), corresponding to high and low electron beam energies, with very different detector rates. The resulting errors on σ_L and σ_T are magnified by $1/\Delta\epsilon = (\epsilon_{Hi} - \epsilon_{Lo})^{-1}$, i.e. there is no error cancellation. To keep the uncertainties in σ_L to an acceptable level, $\Delta\epsilon > 0.2$ is typically required, *i.e.* an uncertainty magnification of no more than 500%. The measurements require continuous, high intensity electron beams, and detectors with good particle identification and reproducible systematics. JLab Hall C is currently the only facility worldwide capable of such studies above $Q^2 = 1$ GeV^2.

Accessing ϵ <0.8 requires $y > 0.5$, which can only occur if s_{tot} is small. For the EIC, this implies low proton collider energies (5-15 GeV), which is well outside the collider design range. Thus, a conventional L/T-separation is impractical at the EIC, and some other way is needed to identify $d\sigma_L/dt$. An alternate approach to reliably estimate σ_L from the measured unseparated cross-sections with the aid of a theoretical model is discussed in Sec. 4.4.

Once $d\sigma_L/dt$ over a range of $-t_{min} < t < 0.3$ GeV^2 has either been measured directly (JLab) or reliably determined (EIC), the value of $F_\pi(Q^2)$ is determined by comparing the $d\sigma_L/dt$ values to the best available electroproduction model of the $ep \to e'\pi^+ n$ reaction. This model must incorporate the effects of the target and recoil nucleons, the off-shell effects of the struck virtual pion in the scattering process, and the contributions of non-pole processes at the measured (Q^2, W, t), where $W^2 = (p_{\pi^+} + p_n)^2$. The model must also have the pion form factor as an adjustable parameter, so that the best-fit value and its uncertainty at fixed (Q^2, W) are obtained by comparison of the

magnitude and t-dependencies of the model and data. To date, three models meeting our criteria are available [4–6]. The obtained F_π values are in principle dependent upon the model used, but one anticipates this dependence to be reduced at sufficiently small $-t$. If several models are available, the form factor values obtained with each one can be compared to better understand the model dependence.

1.3 Importance of EIC measurements

At the EIC, π^+ form factor measurements can be extended to significantly larger Q^2 than possible at JLab. We have written an exclusive $p(e, e'\pi^+ n)$ event generator [7] and performed detailed simulations to determine the feasibility of F_π measurements at the EIC. The key questions we have addressed include: 1) detector requirements to cleanly identify exclusive $e'\pi^+ n$ coincidences; 2) experimental acceptance and projected counting rates for such triple coincidences; 3) event reconstruction resolution requirements to reliably extract $F_\pi(Q^2)$ from $p(e, e'\pi^+ n)$ data. Since the cross section falls rapidly as the distance from the pion pole at $t = m_\pi^2$ is increased, this steep fall off in t needs to be measured to confirm the dominance of the pion cloud mechanism in the acquired data, and the correct treatment of this in the model. This note describes our work addressing these questions and our evaluation of what can be achieved with the EIC in its first five years of running.

2 Simulation Overview

The analysis presented in this note utilises our event generator, DEMPgen [7], in conjunction with the ePIC software stack to produce projections for pion form factor measurements at the EIC. Details on the event generator, simulation and subsequent reconstruction are presented in this section.

2.1 Event Generator Details

DEMPgen version 1.2.4[1] was utilised to generate $p(e, e'\pi^+ n)$ events for this study. DEMPgen events are absolutely-normalized so that project event rates can easily be predicted. This normalization is maintained in the form of an

[1] `https://github.com/JeffersonLab/DEMPgen/releases`

event weighting which is retained through the simulation and reconstruction chain before being applied to final results. Two different early science configurations were studied, namely 10 GeV electron on 130 GeV (10×130) proton and 10 GeV electron on 250 GeV proton (10×250) collisions. Events were generated over the following kinematic range:

- $5 < Q^2 < 35$ GeV^2
- $-t < 0.45$ GeV^2
- $2 < W < 10.2$ GeV

For each beam energy, events were generated in three distinct Q^2 ranges to ensure adequate simulated statistics in each region. These three regions were:

- $5 < Q^2 < 10$ GeV^2
- $10 < Q^2 < 20$ GeV^2
- $20 < Q^2 < 35$ GeV^2

Four hundred thousand events were generated in each Q^2 range for each beam energy combination. Each Q^2 region was selected by imposing a cut on the generation range of scattered electron energies when running the event generator. The resulting output hepmc3 files produced by the generator were processed through the EIC afterburner [8] to apply beam effects. The resulting files were then passed to the ePIC production working group for processing as part of monthly simulation campaigns. Details on how to reproduce the files provided to the production working group, including all simulation input .json cards, can be found here.[2]. The plots presented in subsequent sections show output from the 25.10.2 simulation campaign.

3 Event Selection

DEMP $p(e, e'\pi^+ n)$ events have very well defined kinematics. The scattered electron, e' and produced meson, π^+, are detected by the electron or hadron

[2] `https://github.com/JeffersonLab/DEMPgen/tree/develop/Jul2025_ePIC_Simulation_Campaign`

end caps respectively in most cases, with some events ending up in the central barrel. The neutrons carry the majority of the initial proton beam momentum and as such, are detected in the far forward detectors, primarily the ZDC. The distribution of events for 10×130 and 10×250 events can be seen in Figs. 1 and 2 below.

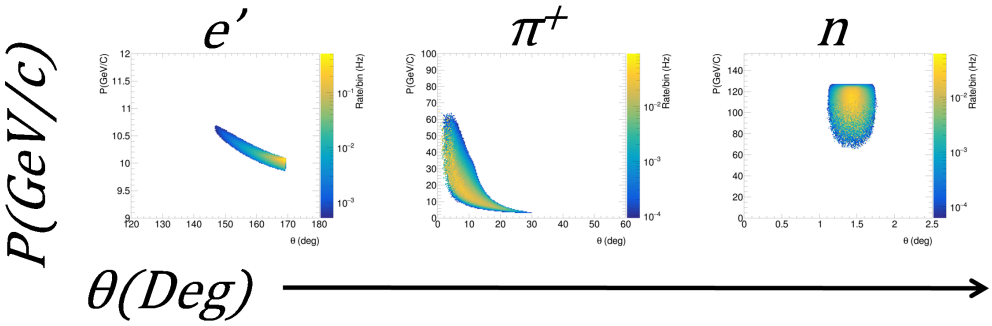

Figure 1: Momentum and polar angle (θ distribution of scattered electrons, e', pions, π^+ and neutrons, n for 10×130 events. Note that the z scale is a rate in Hz due to the absolute normalisation of DEMPgen.

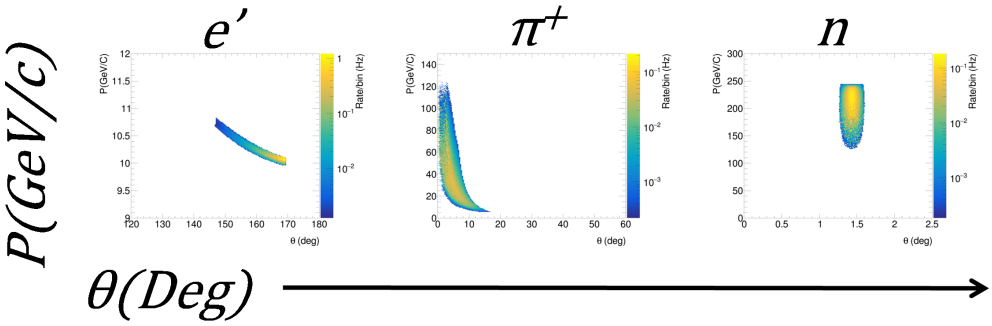

Figure 2: Momentum and polar angle (θ distribution of scattered electrons, e', pions, π^+ and neutrons, n for 10×250 events. Note that the z scale is a rate in Hz due to the absolute normalisation of DEMPgen.

This makes the event selection process relatively straightforward with a clearly defined sequence:

1. Identify charged particles (e' and π^+)
2. Identify neutrons incident on the ZDC
3. Calculate kinematics
4. Apply exclusivity and other cuts

Each stage has some cuts applied which are detailed below.

3.1 Identifying Charged Particles

Due to the distribution of particles in DEMP $p(e, e'\pi^+ n)$ events, the selection of charged particles is very straightforward. The method to identify the scattered electron is based upon the EIC electron finder [9], but is coded in a different style. To identify the scattered electron, the analysis code searches for the highest energy cluster in the barrel electromagnetic calorimeter or the end cap (electron direction) electromagnetic calorimeter. Specifically, the branches "EcalEndcapNClusters' and "EcalBarrelClusters" within EICrecon are searched. The code then checks that the energy of this cluster is $> 0.8 * E_{eBeam}$; if it is lower, the event is discarded. If the cluster is in the barrel, the code also checks that this cluster is in the negative z side (electron going direction) of the calorimeter. Again, if this condition is not met, the event is discarded. This step is staggered such that first the end cap is checked for a good cluster, and if none is found, the barrel is searched.

If a "good" cluster is identified for an event, the code then checks the "ReconstructedChargedParticles" for a track. The code searches for a track with a negative charge, with the track momentum in the $-z$ direction. There is also a requirement that this track has $|\vec{P}|$ greater than 80% of the incident electron beam energy, *i.e.* 8 GeV/c in both beam energy combinations studied in this note. Once a good track and good cluster have been identified, the code then calculates the momentum, P, from a combination of the track and cluster information. This is used to calculate the E/P value for the track plus cluster combination. For real electron signals, this value should be close to ~ 1. As such, a cut is applied on this value and only events with $0.9 < E/P < 1.2$ are retained. If this condition is passed, the track information **only** is assigned to the e' for this event. Calorimeter information is only utilised to veto events and is not used in subsequent calculations.

Note that due to an overlap between the barrel and backwards end cap electromagnetic calorimeters, there is an inefficient region for reconstructing e' clusters of approximately $160° < \theta < 163°$. If no calorimeter cluster is found matching the initial criteria, but a track that passes the selection cuts above is identified with θ in this range, the track information is nonetheless assigned to the e' for this event. This is to compensate for the inefficiency of the calorimeter coverage in this overlap region.

Pion selection currently utilises a slightly simpler approach. The pion is identified by selecting a reconstructed charged particle track with a positive charge and with the track momentum in the $+z$ direction. There is also a requirement that this track has $|\vec{P}|$ greater than 1 GeV/c. This requirement is included to remove any low momentum noise/background events that may be present. Currently, no PID detector is involved to select pions, but incorporating these in future will improve the robustness of this event identification process.

3.2 Identifying Neutrons

For the beam energy combinations studied, the neutron produced in this reaction is incident on, and detected in, the ZDC in almost all generated events. As such, neutron identification is straightforward. Neutrons are identified from the "ReconstructedFarForwardZDCNeutrals" EICrecon branch. To filter out events that are not incident upon the ZDC, and to remove low energy events, cuts are implemented on θ^* and the reconstructed neutral particle energy. θ^* is the polar angle θ after a rotation of 25 mRad around the proton beam axis to remove the effect of the beam crossing angle. After this rotation, the ZDC is indeed, centred at roughly "zero degrees". A cut of $\theta^* < 4\ mRad$ is applied. To remove low energy hits, a cut-off of the neutral particle energy being greater than 40 GeV is applied for 10×130 events. For 10×250 events, this cut off is increased to 120 GeV.

3.3 Calculate Kinematics

Before calculating any kinematic quantities such as Q^2 and $-t$, the analysis code requires that candidate e', π^+ and n that pass relevant selection cuts (as defined above) have been found in coincidence. If this condition is met, the code calculates Q^2, the negative four-momentum transfer squared at the electron vertex. Q^2 can be calculated using various different methods as

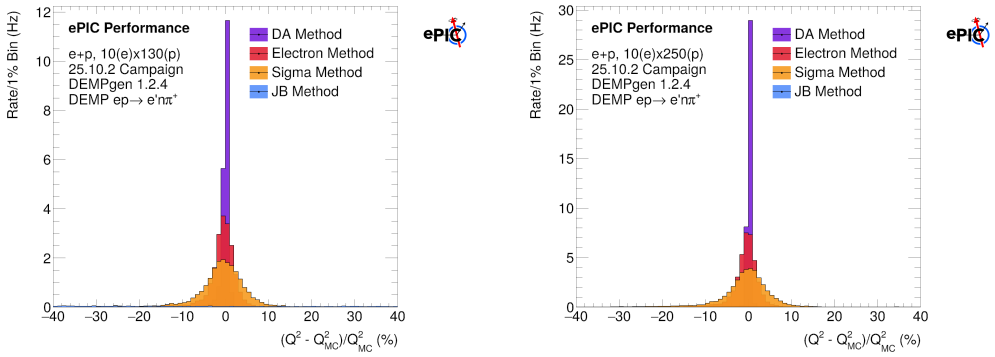

Figure 3: A comparison of the resolution for calculated Q^2 values, defined as the deviation from the MC truth divided by the MC truth value and expressed as a percentage, for 10×130 (left) and 10×250 (right) event samples. Q^2_{DA} is clearly the most accurate in both cases. Note that it is clear that the JB method is not applicable to DEMP kinematics, the distribution for this extends significantly beyond the range of the plot.

discussed here[3]. For the kinematic region under investigation in this study, the double angle (DA) method proved to be optimal, as seen in Fig .3. It is apparent that this calculation method closely matches the "true" value across the relevant Q^2 range (5 to 35 GeV^2), as seen in Fig. 4. Once calculated, a cut on Q^2_{DA} being within 5 and 35 GeV^2 is applied.

Once events outside the relevant Q^2 range are removed, further kinematic quantities are calculated. The squared four-momentum transfer between the initial (p) and final (n) hadron state, t, is critical to determine accurately for DEMP studies. Measurements are needed at the lowest $-t$ possible in order to get as close to the pion pole as possible. As with Q^2, there are many ways to determine t. These are defined in the tRECO convention document [10]. DEMP can utilise the t_{eXBABE} method [11], which exploits the exclusive nature of the reaction to "correct" the measured neutron track. This method outperforms the other reconstruction methods, as seen in Fig. 5. This determination of t also strongly correlates with the MC truth value of t, shown in Fig. 6.

Once calculated, a cut is applied on t. Any events with $0 < -t_{eXBABE} < 1.4$ GeV^2 are removed. Cuts on $W > 0$ GeV and $y_{DA} >$

[3] https://agenda.infn.it/event/43344/contributions/253198/attachments/130672/194493/EIC_KinematicReconstruction.pdf

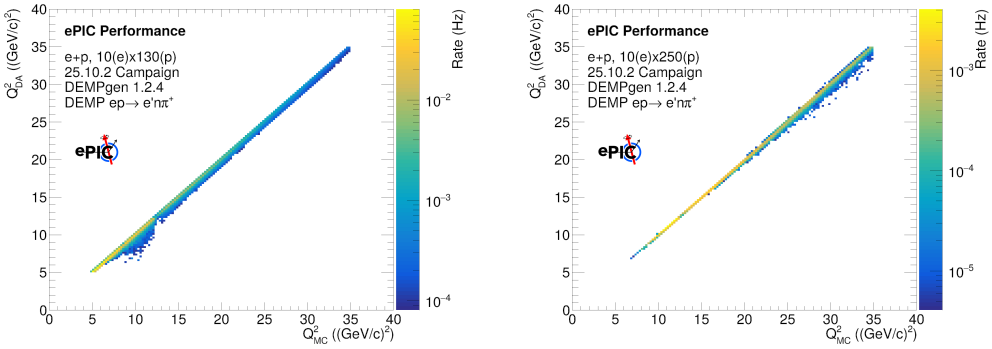

Figure 4: A comparison of Q^2_{DA} against the MC truth value of Q^2 for 10×130 (left) and 10×250 (right) event samples.

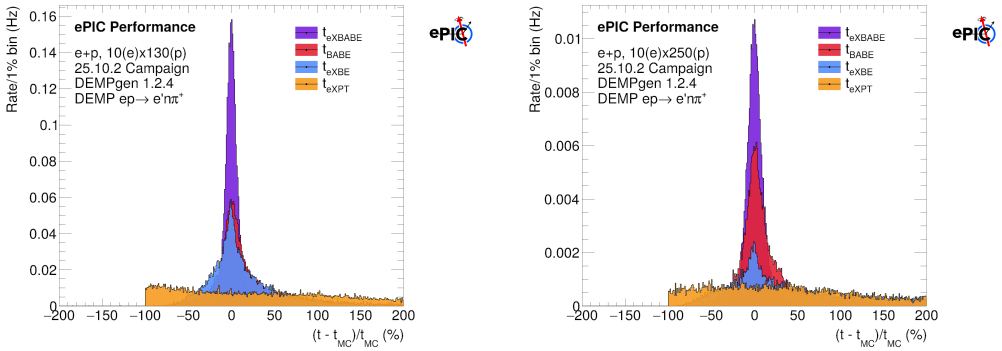

Figure 5: A comparison of the resolution for calculated t values, defined as the deviation from the MC truth divided by the MC truth value and expressed as a percentage, for 10×130 (left) and 10×250 (right) event samples. t_{eXBABE} is clearly the most accurate determination in each case.

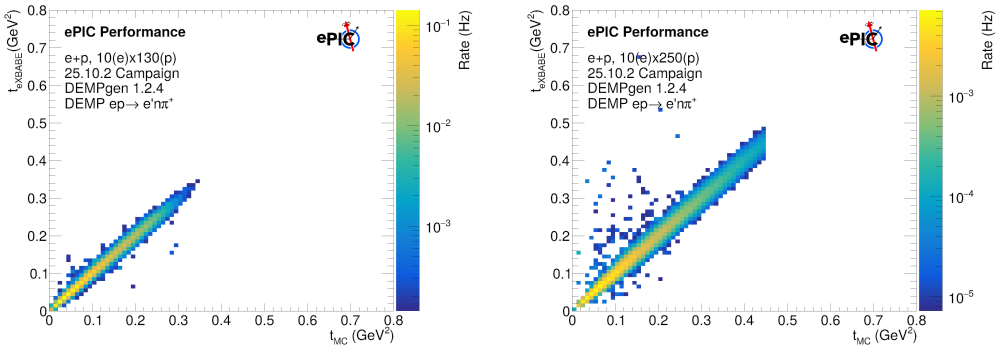

Figure 6: A comparison of $-t_{eXBABE}$ against the MC truth value of $-t$ for 10×130 (left) and 10×250 (right) event samples.

0.01 are also applied, with any events failing these selections being removed. The cut on y_{DA} removes a large number of high weight events as seen in Fig. 7, however, this cut is necessary to remove potential background events at extremely low y. These cuts are applied simultaneously in conjunction with other cuts described in Sec. 3.4.

3.4 Event Selection - Final Cuts

To ensure exclusivity and remove background events, further cuts are needed. This DEMP analysis utilises a somewhat unique cut to achieve these objectives. To implement this cut, a missing momentum 4-vector is determined from the reconstructed e' and π^+ tracks

$$\vec{P}_{Miss} = (\vec{e} + \vec{p}) - (\vec{e}'_{Rec} + \vec{\pi}_{Rec}) \,,$$

where e and p are the initial electron and proton beam 4-vectors, and e'_{Rec}, π_{Rec} are the scattered electron and pion 4-vectors. If this is an exclusive event, the resulting four vector should closely correspond to that of the detected neutron. The polar and azimuthal angles of this track (θ^*_{Miss} and ϕ^*_{Miss}, after rotation by 25 mRad to remove beam crossing effects) should correspond to the polar and azimuthal angles determined from the neutron hit on the ZDC (θ^*_{ZDC} and ϕ^*_{ZDC}, again, after rotation by 25 mRad). Two differences, $\Delta\theta^*$

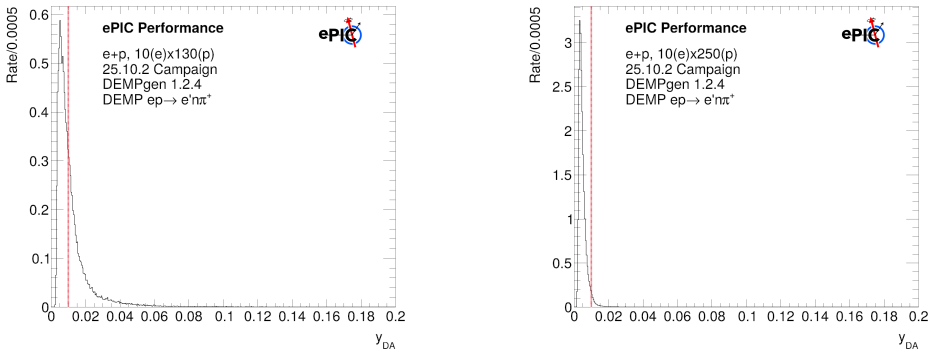

Figure 7: The y_{DA} distribution for 10×130 (left) and 10×250 (right) events with a $5 < Q^2_{DA} < 35$ $(GeV/c)^2$ cut applied. Events with $y_{DA} > 0.1$, anything to the right of the dashed red line in each figure, are removed. This represents a large number of high rate events, but many of these are removed with other cuts. These events are also predominantly at low Q^2.

and $\Delta\phi^*$ can then be defined and calculated as

$$\Delta\theta^* = \theta^*_{pMiss} - \theta^*_{ZDC},$$
$$\Delta\phi^* = \phi^*_{PMiss} - \phi^*_{ZDC}.$$

For exclusive events, these differences should be very small, particularly $\Delta\theta^*$ due to the excellent position resolution of the ZDC[4]. As such, only events satisfying

$$-0.09^\circ < \Delta\theta^* < 0.14^\circ,$$
$$-55^\circ < \Delta\phi^* < 55^\circ,$$

for 10×130 events and

$$-0.07^\circ < \Delta\theta^* < 0.17^\circ,$$
$$-80^\circ < \Delta\phi^* < 80^\circ,$$

for 10×250 events are retained. These ranges were chosen along lines of constant rate in a plot of $\Delta\theta^*$ vs $\Delta\phi^*$, such as in Fig. 8, to minimize variations across the acceptance of the ZDC. They were also chosen to be conservative,

[4]Note that $\Delta\phi^*$ is spread over a broader range as it only utilises the x and y components of the 4-vector which are smaller and less accurately determined than the z component

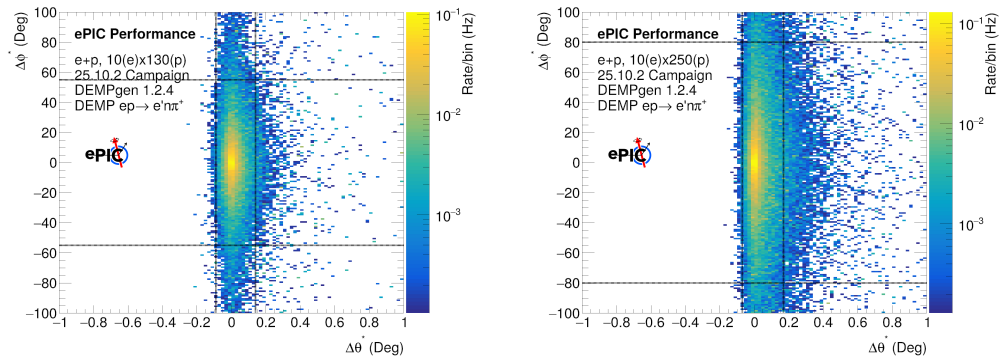

Figure 8: $\Delta\theta^*$ vs $\Delta\phi^*$ for 10×130 (left) and 10×250 (right) events. Note that as only DEMP events are processed, the majority of events survive this cut. Cuts were chosen along lines of constant rate as the peak area of the distribution tails off, as indicated by the dashed black lines showing the cut region. Events outside of the shape confined by these four lines are removed.

as SIDIS or other background events, which should not reconstruct in this range, will be excluded. For non-exclusive events, the missing momentum vector should not correspond to a single particle, and as such, $\Delta\theta^*$ and $\Delta\phi^*$ should be spread across a much broader range. This is readily apparent in Fig. 9 which shows that for DIS events, which pass equivalent selection cuts to those used in Fig. 8, very few events lie within the cut regions selected.

This cut is an indirect cut on the missing momentum and, as a consequence, the missing energy. However, to further reduce any potential background events leaking in, a further, direct cut on the missing momentum is applied. The missing momentum for the full DEMP system is calculated as

$$\vec{P}_{M\_DEMP} = (\vec{e} + \vec{p}) - (\vec{e\prime}_{Rec} + \vec{\pi}_{Rec} + \vec{n}_{Rec})\,.$$

Cuts are applied on the $.M2()$ and $.M()$ values of this 4-vector. Events with:

$$\vec{P}_{M\_DEMP}.M2() < -1\ \left(\mathrm{GeV/c^2}\right)^2,$$
$$\vec{P}_{M\_DEMP}.M() > 0.75\ \mathrm{GeV/c^2},$$

respectively are removed. This is to account for the fact that for a true exclusive event, all particles in the event should be detected and as such, the "missing" mass should be ≈ 0. These cuts are shown in Figs. 10 and 11, respectively.

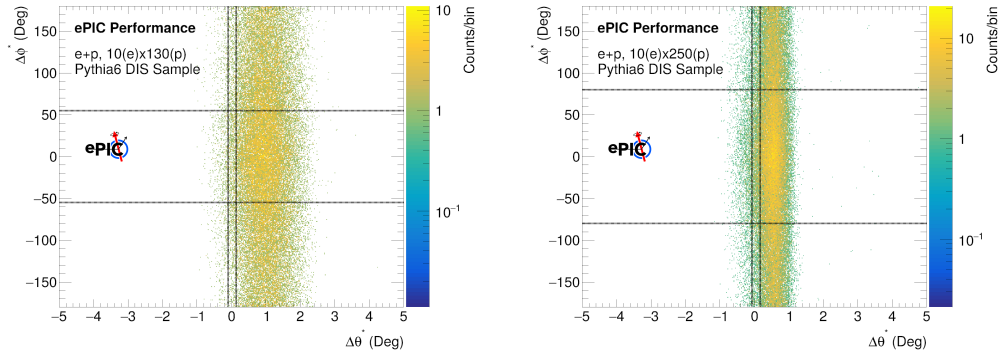

Figure 9: $\Delta\theta^*$ vs $\Delta\phi^*$ for 10×130 (left) and 10×250 (right) DIS events. Note that the axis ranges are significantly broader than in Fig.8. Very few events lie within the region enclosed within the dashed black lines. The analysis of the background contribution from DIS events is discussed further in Sec.4.1.

Finally, a cut on the sum of $E - P_z$ for all detected final state particles is applied. In the absence of initial state radiation or background events, this sum should be roughly equal to two times the electron beam energy (20 GeV in each case under study here). As such, a cut of

$$18 < \sum (E - P_z) < 22 \text{ GeV}$$

is applied. Again, as no initial state radiation is included in DEMPgen and no background events are included in the event sample, this range has been chosen to be conservative. This cut range will be adjusted as these effects are incorporated in future studies.

3.5 Analysis Code

The analysis of processed DEMP events is via a standard ROOT/C++ based macro. The analysis code is stored on GitHub and can be accessed here[5]. This repository also contains some utility scripts that can be used to cut down the size of the reconstructed simulation output if desired.

[5] `https://github.com/sjdkay/ePIC_DEMP_Analysis/blob/main/DEMP_Analysis.C`

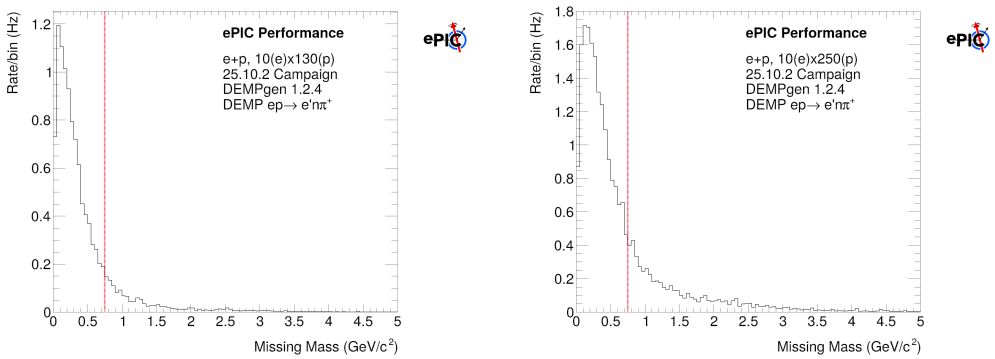

Figure 10: The $\vec{P}_{M\_DEMP}.M()$ distribution for 10×130 (left) and 10×250 (right) events. Events with $\vec{P}_{M\_DEMP}.M() > 0.75\text{GeV/c}^2$, anything to the right of the dashed red line in each figure, are removed.

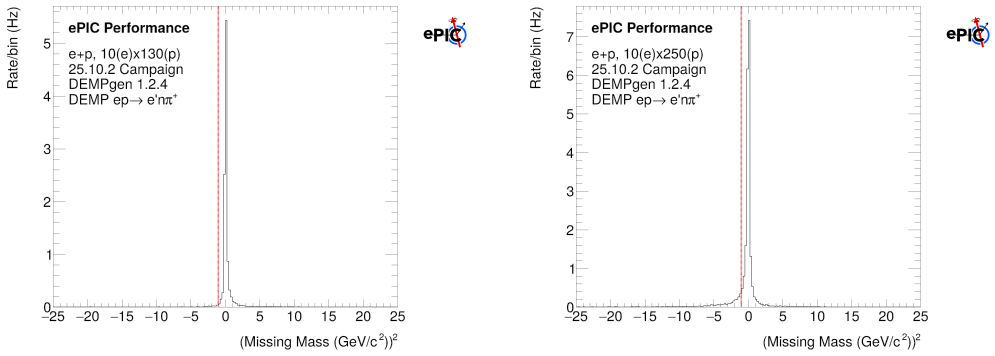

Figure 11: The $\vec{P}_{M\_DEMP}.M2()$ distribution for 10×130 (left) and 10×250 (right) events. Events with $\vec{P}_{M\_DEMP}.M2() < -1\left(\text{GeV/c}^2\right)^2$, anything to the left of the dashed red line in each figure, are removed.

4 Results and Discussion

4.1 DIS Leakthrough

DIS events are likely to be the dominant physics process detected at the EIC. Some DIS events may "mimic" signals from exclusive channels. To test how many events of this type might leakthrough into the analysis of exclusive $p(e, e'\pi^+ n)$ events, a sample of DIS events was processed through the analysis code and cuts described above. All cuts were kept identical for a given beam energy. A sample of 10x130 and 10x250 PYTHIA 6 neutral current DIS events was processed in this manner. After all cuts and selection criteria were applied, only ∼0.01% of DIS events remained for 10x130 and 10x250 respectively. Remaining events were also predominantly at lower Q^2 where DEMP event rates are higher. This provides confidence that the selection cuts utilised can adequately isolate exclusive $p(e, e'\pi^+ n)$ events.

4.2 Statistical Uncertainties

For the purpose of the statistical uncertainties, our projections are for an integrated luminosity of $5.0\times10^{39}/\text{cm}^2$. For 10×130 beam energy combination, an instantaneous luminosity of $2.53\times10^{32}/\text{cm}^2/\text{s}$ corresponds to a running time of 1.9×10^7s (220 days) with 100% data taking efficiency. The triple-coincidence $p(e, e'\pi^+ n)$ events analyzed in the above manner were binned in Q^2 and t, with default bin widths of ΔQ^2=1 GeV^2 and $\Delta t = 0.02$ GeV^2. An example of the rates per bin for events in a low Q^2 bin can be seen in Fig. 12. This binning width was applied to all except the highest Q^2 data, where the Q^2-bin width was widened to provide sufficient statistics in those bins.

It is vital that the (Q^2, t)-binning be at least as wide as the t reconstruction resolutions shown in Figs. 4, 6, as significant bin migration will significantly hamper the theoretical interpretation of the results. This is unlikely to be an issue for Q^2 binning, as the resolution varies from ∼0.02 to 0.35 GeV^2 across the $5-35$ GeV^2 range considered for 10×130 and 10×250 events, as shown in Figs. 13, 14 respectively. This is comfortably within the 1 GeV^2 width of Q^2 bins that was chosen.

For t, the situation is slightly more complex. The t resolution ranges from 0.002–0.02 GeV^2 for 10×130 in the $-t < 0.2$ GeV^2 range. For 10×250 , the corresponding resolution range is 0.01–0.025 GeV^2 for the same range in t. In both cases, the resolution worsens (i.e. the RMS width gets larger)

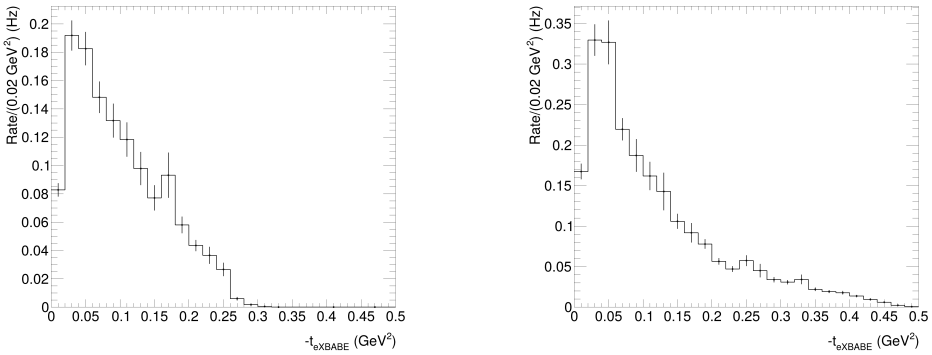

Figure 12: The rates per 0.02 GeV^2 t bin for 10×130 (left) and 10×250 (right) events in the $5 < Q^2 < 6$ GeV^2 bin.

with $-t$ as shown in Figs. 15, 16. For the lowest 5 $-t$ bins that are used in the extraction of F_π, the resolution is smaller than the chosen 0.02 GeV^2 bin width in the majority of cases. This situation also varies by Q^2 bin, as discussed in the Appendix A. For higher Q^2 bins and for higher beam energy combinations, broader $-t$ bins may be needed to avoid a large bin migration correction, as was the case with HERMES [12].

To minimize statistical uncertainties, events were integrated over the full W range covered by the data in the (Q^2, t) bin. We have not yet tested whether additional binning in W will be needed to constrain the additional theoretical uncertainties discussed in Sec. 4.4, but this is a likely possibility.

4.3 Assumed systematic uncertainties on the cross section

The extraction of pion form factor information from the $p(e, e'\pi^+n)$ data set requires that the measured $d\sigma/dt$ have small systematic uncertainties in both their absolute normalization, and in their $(Q^2, W, t, \theta^*, \phi)$ kinematic placement. There are no previous measurements in the EIC kinematic region to use as a reference. The JLab Hall C $p(e, e'\pi^+)n$ data are taken with high resolution focusing magnetic spectrometers in a fixed target environment, which will yield very different systematics than ePIC. H1@HERA was unable to cleanly isolate the exclusive π^+ process, but did publish inclusive leading neutron $p(e, e'n)X$ data that was used to infer the pion structure function F_1^π [13]. HERMES@HERA published unseparated $p(e, e'\pi^+)n$ cross

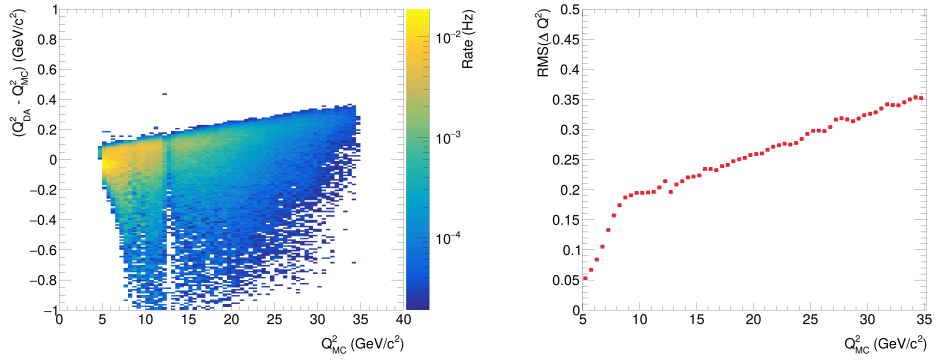

Figure 13: (Left) $\Delta Q^2 = Q^2_{MC} - Q^2_{DA}$ as a function of Q^2_{MC} for 10×130 events. The RMS widths of these slices are plotted as a function of the bin centroid in Q^2_{MC} in the (Right) figure. The y-axis can be interpreted as the resolution in Q^2.

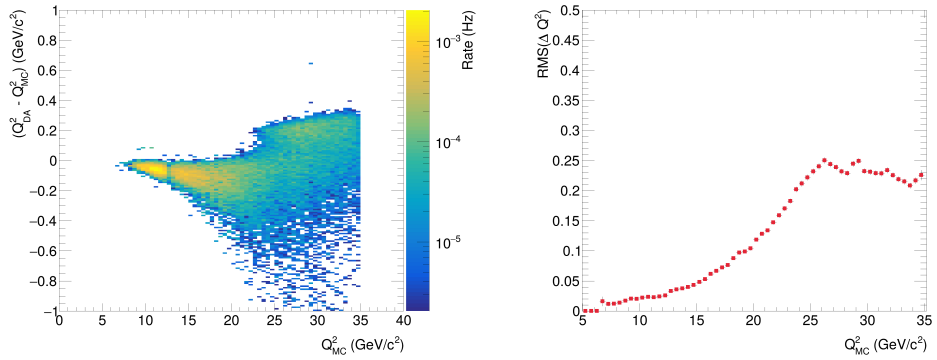

Figure 14: (Left) $\Delta Q^2 = Q^2_{MC} - Q^2_{DA}$ as a function of Q^2_{MC} for 10×250 events. The RMS widths of these slices are plotted as a function of the bin centroid in Q^2_{MC} in the (Right) figure. The y-axis can be interpreted as the resolution in Q^2.

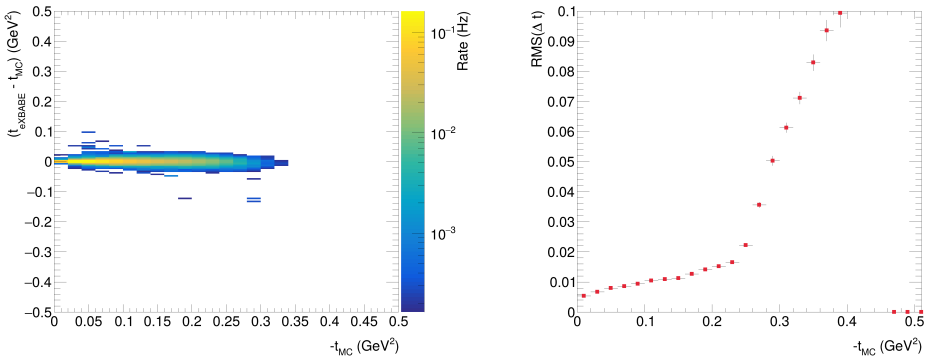

Figure 15: (Left) $\Delta t = t_{mc} - t_{eXBABE}$ as a function of $-t_{MC}$ for 10×130 events across all Q^2_{DA} bins. One bin wide slices along the x-axis are taken from this figure. The RMS widths of these slices are plotted as a function of the bin centroid in $-t_{MC}$ in the (Right) figure. The y-axis can be interpreted as the resolution in $-t$. The sharp rise above $t_{MC} \sim 0.25$ GeV^2 demonstrates the fall off in ZDC acceptance at the edges of the detector, rather than a sudden decrease in resolution.

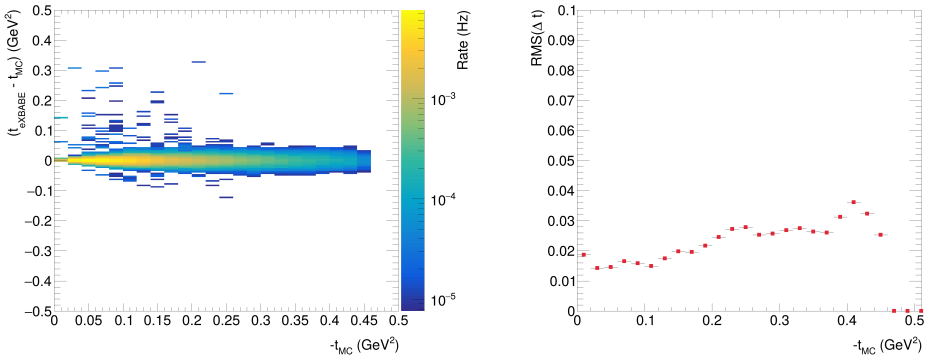

Figure 16: (Left) $\Delta t = t_{mc} - t_{eXBABE}$ as a function of $-t_{MC}$ for 10×250 events across all Q^2_{DA} bins. One bin wide slices along the x-axis are taken from this figure. The RMS widths of these slices are plotted as a function of the bin centroid in $-t_{MC}$ in the (Right) figure. The y-axis can be interpreted as the resolution in t.

sections, where a missing mass cut $M_X^2 < 1.2$ GeV^2 selected an event sample dominated by exclusive events [12]. In the HERMES measurement, the systematic uncertainty for the number of exclusive events ranged from 5-20% depending on the t-bin, with additional systematic uncertainties of $< 15\%$ in the acceptance of the spectrometer, $<25\%(35\%)$ in bin-migration out(in) of a given exclusive event bin, and 5% in integrated luminosity normalization. For this study, we assume cross-section systematic uncertainties similar to those of the H1@HERA pion structure function measurement [13]), which is the closest comparable study. This leads to assumed cross-section systematic uncertainties of 2.5% point-to-point and 12% scale.

4.4 Assumed systematic uncertainties coming from the L/T-separation

After the exclusive $p(e, e'\pi^+ n)$ event sample is identified, the next step is to separate the longitudinal cross-section $d\sigma_L/dt$ from $d\sigma_T/dt$, needed for the extraction of the pion form factor. However, due to the lack of low ϵ data, a conventional Rosenbluth separation (Eqn. 1) is impractical at the EIC. Fortunately, at the high Q^2 and W accessible at the EIC, phenomenological models predict $\sigma_L \gg \sigma_T$ at small $-t$. This is expected, since in the hard scattering regime QCD scaling predicts $\sigma_L \propto Q^{-6}$ and $\sigma_T \propto Q^{-8}$, hence σ_L is expected to dominate at sufficiently high Q^2. For example, the Vrancx and Ryckebusch (VR) Regge-based model [14] predicts $R = \sigma_L/\sigma_T > 10$ for $Q^2 > 10$ GeV^2 and $-t < 0.06$ GeV^2, and $R > 25$ for $Q^2 > 25$ GeV^2 and $-t < 0.10$ GeV^2. As shown in Fig. 17, the transverse cross-section contributions are expected in these cases to be only 4-10% of σ_{uns}. The most practical choice appears to be to use a model to isolate the dominant $d\sigma_L/dt$ from the measured $d\sigma_{uns}/dt$.

Since a model will be solely responsible for the subtraction of σ_T from the experimental data to yield σ_L, it will be very important to confirm the validity of the model used. This can also be done with EIC data, using exclusive ${}^2H(e, e'\pi^+ n)n$ and ${}^2H(e, e'\pi^- p)p$ data at the same kinematics as the primary $p(e, e'\pi^+ n)$ measurement. The ratio of these cross sections is

$$R_{\pm} = \frac{\sigma[n(e, e'\pi^- p)]}{\sigma[p(e, e'\pi^+ n)]} = \frac{|A_V - A_S|^2}{|A_V + A_S|^2} \tag{2}$$

where A_V is the isovector amplitude, and A_S is the isoscalar amplitude. Since the pion pole t-channel process used for the determination of the pion

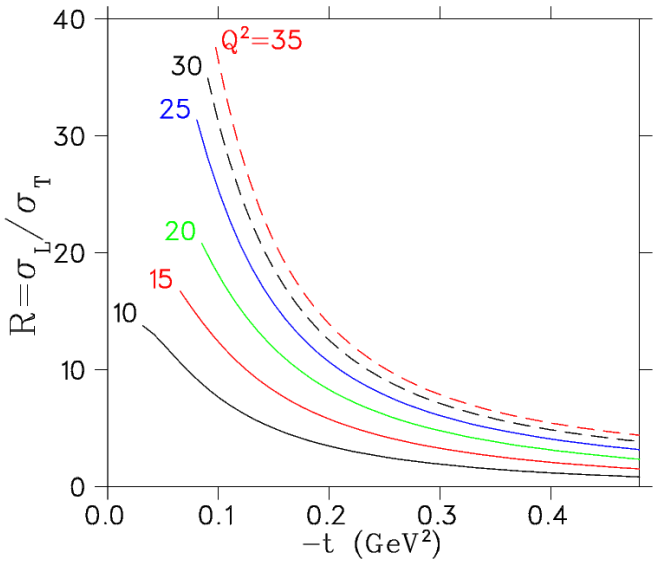

Figure 17: VR model [14] predictions for $R = \sigma_L/\sigma_T$ versus t for kinematics typical of the EIC. The curves range from Q^2=10 GeV^2 (lowest), W=7.0 GeV to Q^2 =35 GeV^2, W=9.5 GeV (highest). For all of these kinematics $\epsilon > 0.995$.

form factor is purely isovector (due to G-parity conservation), the above ratio will be diluted if σ_T is not small, or if there are significant non-pole contributions to σ_L. The comparison of the measured π^-/π^+ ratio to model expectations, therefore, provides an effective means of validating the model used to determine σ_L. The same model, now validated, can likely also be used to extract the pion form factor from the σ_{uns} data.

Fig. 18 presents a prediction of such ratios using the VR Regge model for typical EIC kinematics. We have not yet had an opportunity to simulate the $^2H(e,e'\pi^+n)n$, $^2H(e,e'\pi^-p)p$ processes for EIC early science running. We plan to do so once the personnel hired to work on the necessary extensions to the DEMPgen generator arrives in Canada. Demonstrating the feasibility of such measurements with ePIC are clearly essential for the EIC meson form factor program.

Any published F_π results from the EIC will need to assign a systematic uncertainty to the use of the model used to isolate σ_L from the $d\sigma/dt$ data. In the actual EIC experiment, this uncertainty can be determined from the detailed comparison of model and e+^{2}H data for $R_\pm$ above. In the meantime, we have assumed an uncertainty of $\delta r = r = 0.013 - 0.15$, where $r = 1/R =$

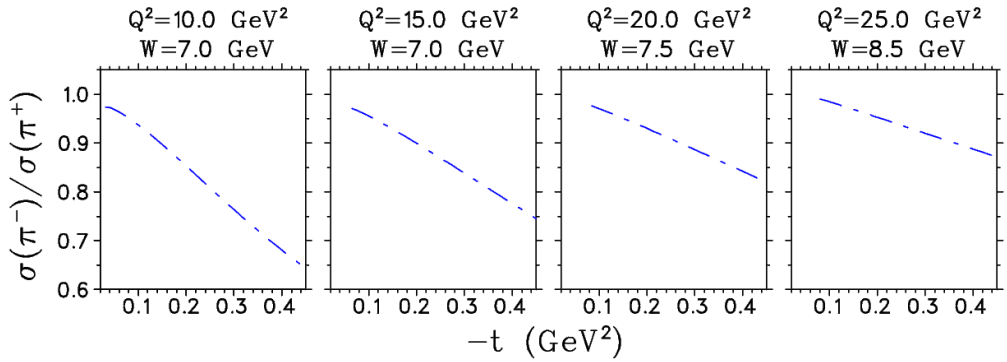

Figure 18: VR model [14] predictions for $R_{\pm}$ versus t for kinematics typical of the EIC. As expected the ratio is near unity at $-t_{min}$ and drops rapidly thereafter, due to the presence of non-pion-pole contributions to the cross-section. Comparisons of such ratios with experimental data will be essential for confirming the validity of the model used to infer $F_\pi(Q^2)$ from the experimental cross-sections.

σ_T/σ_L. As seen in Fig. 17, this uncertainty will be largest for Q^2 =5-10 GeV^2, and much smaller for Q^2 >20 GeV^2.

4.5 Projected F_π uncertainties and kinematic reach

Once triple-coincidence $p(e, e'\pi^+ n)$ events are cleanly identified with ePIC, the value of $F_\pi(Q^2)$ is determined by comparing the measured $d\sigma_L/dt$ values at small $-t$ to the electroproduction models. Measurements over a range of $-t$ are an essential part of the model validation process, to confirm that the model is able to correctly reproduce not only the magnitude of the cross-section, but also its t-dependence. The JLab 6 GeV experiments were instrumental in establishing the reliability of this technique up to $Q^2 = 2.45$ GeV^2 [3, 15–22], and extensive further tests are planned as part of JLab experiment E12-19-006 [23]. The JLab experiments had to estimate an additional model uncertainty coming from the form factor extraction fit to the data. We do not assign any such uncertainty here, but the EIC should provide data over a sufficiently large kinematic range to allow the model dependence to be quantified in a detailed analysis.

The assumed statistical and systematic uncertainties are given in Table 1 for two 10×130 Q^2-bins, one with good statistics, and the other with poorer statistics. These uncertainties include the assumed experiment systematics

$10.0 \leq Q^2 < 11.0$ GeV^2, $\overline{Q^2}$=10.50 GeV^2, $\overline{W}$=9.09 GeV, $-t_{min}$=0.02 GeV^2

$-t_{bin}$	$r = T/L$	$\frac{Counts}{t-\phi\ bin}$	$\delta\sigma_{uns}$	$\delta\sigma_{L\ (stat+uncorr)}$	$\delta\sigma_{L\ (t-corr+scale)}$
0.03	7.5%	38000	2.55%	2.86%	13.88%
0.05	8.8%	39600	2.55%	2.99%	14.45%
0.07	10.0%	34700	2.56%	3.15%	15.06%
0.09	12.6%	25900	2.58%	3.54%	16.41%
0.11	15.2%	20400	2.60%	4.00%	17.84%
δF_π from 5 lowest t-bins: 1.62% (stat+uncorr), 4.50% (δr), 6.0% (scale), 7.27% (incl t-corr+scale)					

$25.0 \leq Q^2 < 28.0$ GeV^2, $\overline{Q^2}$=26.50 GeV^2, $\overline{W}$=9.18 GeV, $-t_{min}$=0.07 GeV^2

$-t_{bin}$	$r = T/L$	$\frac{Counts}{t-\phi\ bin}$	$\delta\sigma_{uns}$	$\delta\sigma_{L\ (stat+uncorr)}$	$\delta\sigma_{L\ (t-corr+scale)}$
0.09	3.5%	6030	2.81%	2.84%	12.47%
0.11	4.4%	6140	2.81%	2.88%	12.73%
0.13	5.3%	5080	2.82%	2.95%	13.03%
0.15	6.4%	4880	2.88%	3.08%	13.44%
0.17	7.5%	4190	2.94%	3.23%	13.90%
δF_π from 5 lowest t-bins: 1.49% (stat+uncorr), 2.33% (δr), 6.0% (scale), 6.57% (incl t-corr+scale)					

Table 1: Detailed error calculation for two Q^2 points with 10×130 beam energy combination. The estimated $r = T/L$ values are taken from the VR model [14], and we take the uncertainty in the ratio as $\delta r = r$. The simulated number of experimental counts/bin are for an integrated luminosity of 5×10^{39}/cm^2. The uncertainty in the unseparated cross section $\delta\sigma_{uns}$ includes both statistical and an estimated uncorrelated systematic uncertainty of 2.5%, added in quadrature. The next column, $\delta\sigma_L$(stat+uncorr), propagates this uncertainty to σ_L using Eqn. 3. $\delta\sigma_L$(t-corr+scale) shows the non-statistical errors, including the assumed 12% scale systematic uncertainty in the cross section measurement, also propagated from σ_{uns} to σ_L. The uncertainty in the pion form factor is based on both of these errors, as described in the text. The first uncertainty corresponds to the inner error bar in Fig. 19, while the fourth uncertainty is the outer error bar.

discussed in Sec. 4.3, and the uncertainties from the use of a model to isolate σ_L discussed in Sec. 4.4. If we take $LT = TT = 0$, we can invert Eqn. 1 to give $\sigma_L = \sigma_{uns}/(r+\epsilon)$, and

$$\delta\sigma_L = \sqrt{\left(\frac{\delta\sigma_{uns}}{r+\epsilon}\right)^2 + \left(\frac{\delta r}{r+\epsilon}\right)^2}, \tag{3}$$

assuming the uncertainty in ϵ is small enough to be ignored.

The propagation of these uncertainties to F_π is as follows. Since the Born term model of Actor, Korner and Bender [24] predicts the pion-pole contribution to σ_L to be

$$N\frac{d\sigma_L}{dt} = 4\hbar c\ (eg_{\pi NN})^2\ \frac{-t}{(t-m_\pi^2)^2}\ Q^2F_\pi^2(Q^2), \tag{4}$$

where $e^2/(4\pi\hbar c) = 1/137$ and N depends on the virtual photon flux factor, it is reasonable to assume $F_\pi \propto \sqrt{\sigma_L}$, *i.e.* $\delta F_\pi = \delta\sigma_L/2$. The final F_π uncertainties achieved in the JLab experiment [18] are best modelled by taking the geometric mean of the statistical and uncorrelated systematic errors of the lowest 5 t-bins used in the form factor extraction from σ_L data, added in quadrature to the t-correlated and scale uncertainties of the lowest $-t$-bin. Table 1 shows also for the δr and scale uncertainty contributions to F_π (taken from the lowest 5 t-bins), for comparison. These give the final uncertainties in F_π of about 7% for both the low and high statistics Q^2-bins in the table.

Projected uncertainties and kinematic reach of an early science pion form factor measurement are shown in Fig. 19. Note that the 10×250 setting does not extend as low in Q^2 as the 10×130 setting, primarily due to the applied $y > 0.01$ cut. Regarding the projected uncertainties, for the lowest Q^2 bins ($Q^2 < 10$ GeV^2) the uncertainty in r is among the larger systematic uncertainties, arising the relatively less favorable T/L ratio. At intermediate Q^2 ($10 < Q^2 < 25$ GeV^2), the $r = T/L$ ratio is more favorable and the experimental systematic uncertainties dominate. The statistical uncertainties are largest for the Q^2 >25 GeV^2 bins, as the rates there are much lower. The width of the highest Q^2 bins has been increased to allow a minimum threshold of ∼3000 $e\pi^+n$ coincidences for the lowest 5 t-bins at each Q^2. This gives similar statistical uncertainties as those obtained with the default $\Delta Q^2 = 1$ GeV^2 binning at intermediate Q^2. It is difficult to know at this stage whether this wider Q^2-binning will introduce additional systematic uncertainties elsewhere in the form factor extraction.

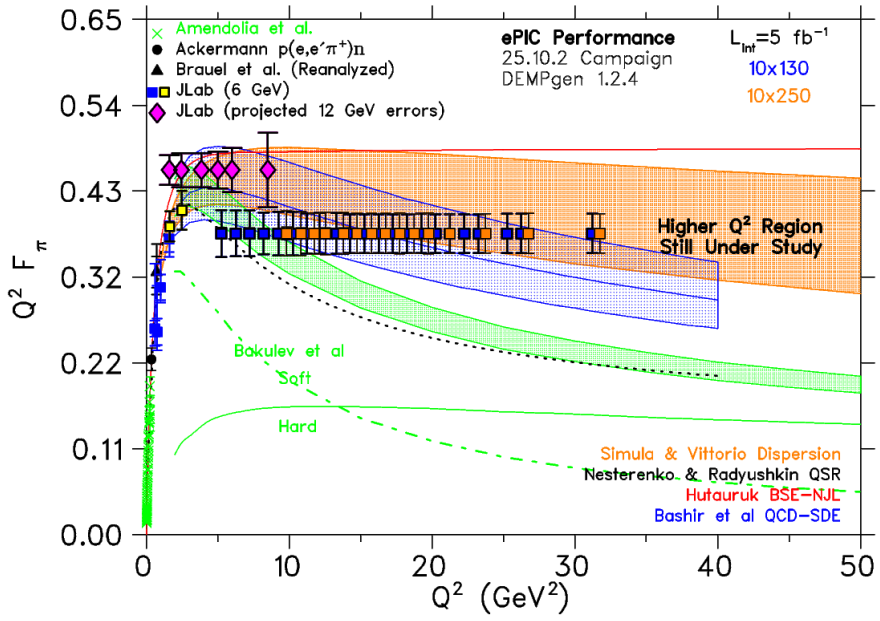

Figure 19: Existing data (blue, black, yellow, green) and projected uncertainties for future data on the pion form factor from JLab (magenta) and ePIC (blue, orange), in comparison to a variety of hadronic structure models. The projected ePIC data have double error bars, where the inner error bar includes only statistical and assumed point-to-point systematic errors, and the outer error bar includes also the correlated systematic errors.

It is clear that with these assumptions, the pion form factor projections in Fig. 19 are systematics limited over the full kinematic range. If additional W binning is required (as mentioned in Sec. 4.2), the statistical limitations of the data will be more pronounced. The projections stop at $Q^2 = 35$ GeV^2 due to the limitations of DEMPgen. When we started working on the generator, we did not anticipate the possibility of acquiring significant EIC data above $Q^2 > 35$ GeV^2. Given that this may be possible, we plan to extend DEMPgen to at least Q^2=50 GeV^2 in the future.

4.6 Conclusion

To conclude, the extraction of the pion form factor to high Q^2 with ePIC depends on very good ZDC angular resolution for two reasons: 1) the necessity to separate the small exclusive π^+ cross-section from dominant inclusive

backgrounds via $\Delta\theta^*$ and $\Delta\phi^*$ cuts, 2) the need to reconstruct t to better than $\sim$0.02 GeV^2, such resolution is only possible when reconstructed from the initial proton and final neutron momenta. The performance of the ePIC far forward detectors is thus of crucial importance to the feasibility of a pion form factor measurement.

5 Acknowledgments

This work is supported by the Natural Sciences and Engineering Research Council of Canada (NSERC) grants SAPIN-2021-00026 and SAPPJ-2025-00040, and the UK Research and Innovation Science and Technology Facilities Council (STFC).

A t Resolutions

As discussed in Sec. 4.2, the resolution in t varies with beam energy and across Q^2 bins, as shown in Figs. 20–25. For 10×130 events, the resolution in t is comfortably within the chosen width of each bin for the range of t that is used in the form factor determination. The exception to this is for high $-t$ values in higher Q^2 bins, as can be seen in Fig. 22. As such, for the high Q^2 bins at this beam energy, either broader t bins must be used, or a bin-migration systematic will need to be applied.

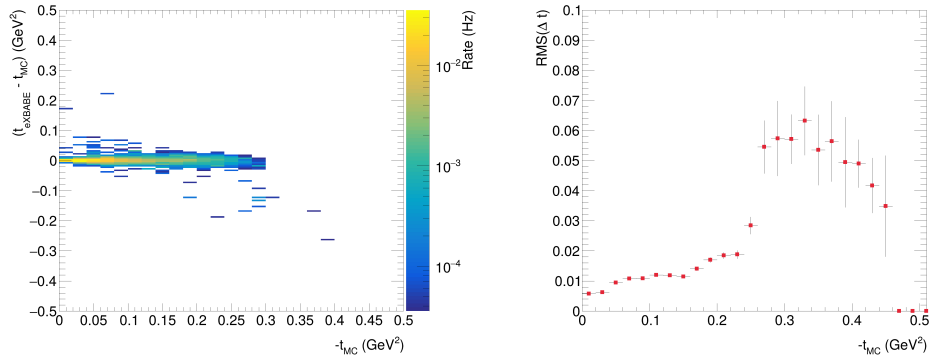

Figure 20: (Left) $\Delta t = t_{mc} - t_{eXBABE}$ as a function of $-t_{MC}$ for 10×130 events with $5 < Q^2_{DA} < 6$ GeV^2. One bin wide slices along the x-axis are taken from this figure. The RMS widths of these slices are plotted as a function of the bin centroid in $-t_{MC}$ in the (Right) figure. The y-axis can be interpreted as the resolution in t.

For 10×250 events, the situation is more nuanced. Wider t bins may be needed even at modest Q^2, such as in Fig.21 or a potentially substantial bin migration systematic may be needed. It is clear that due to selection cuts, very low Q^2 bins, such as in Fig. 20, are effectively removed in this setting.

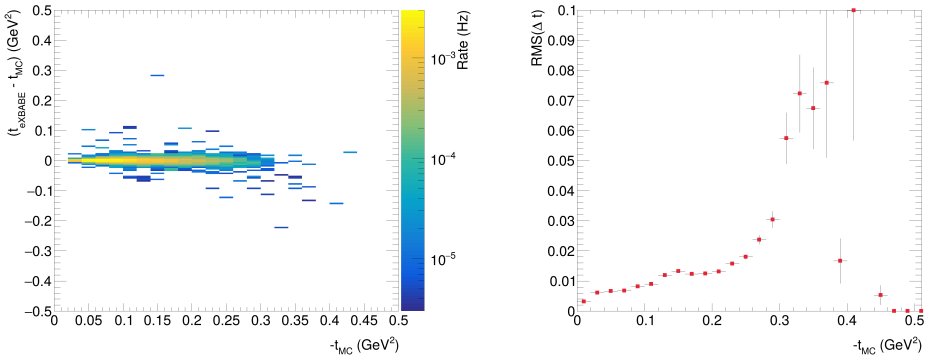

Figure 21: (Left) $\Delta t = t_{mc} - t_{eXBABE}$ as a function of $-t_{MC}$ for 10×130 events with $17 < Q^2_{DA} < 18$ GeV^2. The RMS widths of these slices are plotted as a function of the bin centroid in $-t_{MC}$ in the (Right) figure. The y-axis can be interpreted as the resolution in t.

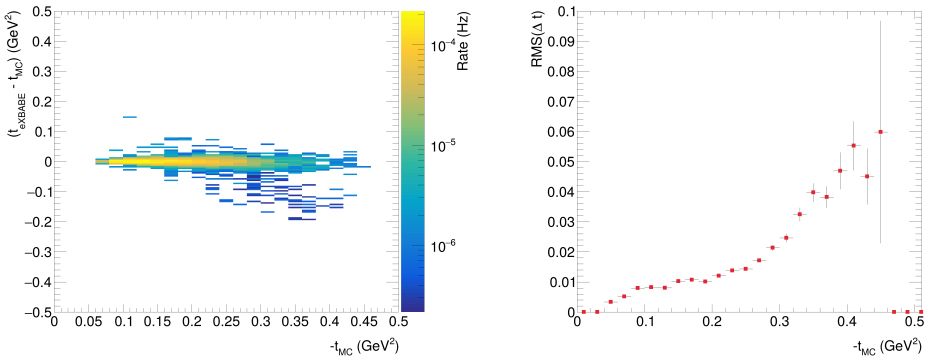

Figure 22: (Left) $\Delta t = t_{mc} - t_{eXBABE}$ as a function of $-t_{MC}$ for 10×130 events with $32 < Q^2_{DA} < 33$ GeV^2. The RMS widths of these slices are plotted as a function of the bin centroid in $-t_{MC}$ in the (Right) figure. The y-axis can be interpreted as the resolution in t.

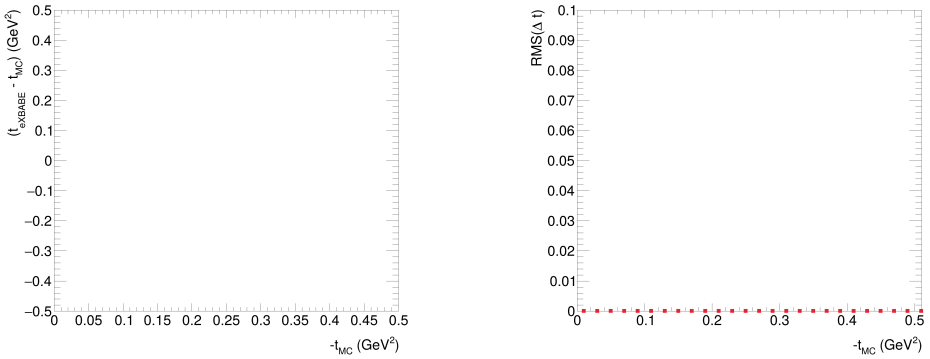

Figure 23: (Left) $\Delta t = t_{mc} - t_{eXBABE}$ as a function of $-t_{MC}$ for 10×250 events with $5 < Q^2_{DA} < 6$ GeV^2. **Due to selection cuts, this bin is not viable for 10×250.**

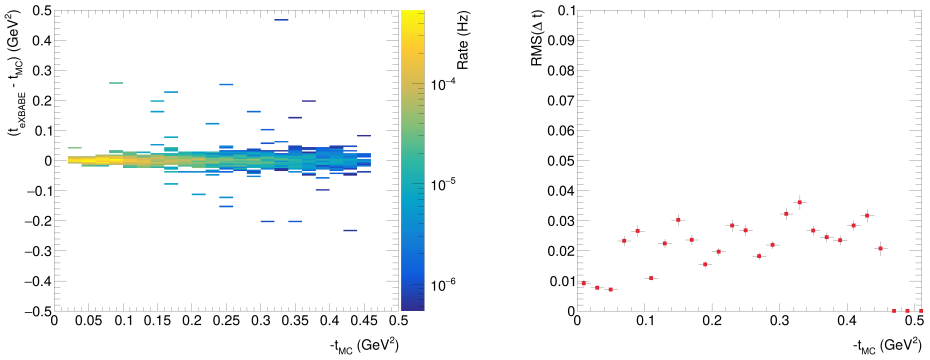

Figure 24: (Left) $\Delta t = t_{mc} - t_{eXBABE}$ as a function of $-t_{MC}$ for 10×250 events with $17 < Q^2_{DA} < 18$ GeV^2. The RMS widths of these slices are plotted as a function of the bin centroid in $-t_{MC}$ in the (Right) figure. The y-axis can be interpreted as the resolution in t.

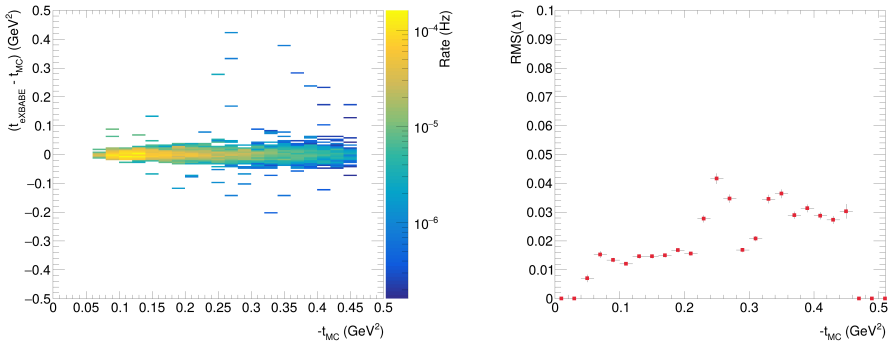

Figure 25: (Left) $\Delta t = t_{mc} - t_{eXBABE}$ as a function of $-t_{MC}$ for 10×250 events with $32 < Q^2_{DA} < 33$ GeV^2. The RMS widths of these slices are plotted as a function of the bin centroid in $-t_{MC}$ in the (Right) figure. The y-axis can be interpreted as the resolution in t.

References

[1] G. Peter Lepage, S. J. Brodsky, Exclusive processes in quantum chromodynamics: Evolution equations for hadronic wavefunctions and the form factors of mesons, Physics Letters B 87 (4) (1979) 359–365. doi:https://doi.org/10.1016/0370-2693(79)90554-9.
URL https://www.sciencedirect.com/science/article/pii/0370269379905549

[2] F. Gao, L. Chang, Y.-X. Liu, C. D. Roberts, P. C. Tandy, Exposing strangeness: projections for kaon electromagnetic form factors, Phys. Rev. D 96 (3) (2017) 034024. arXiv:1703.04875, doi:10.1103/PhysRevD.96.034024.

[3] T. Horn, C. D. Roberts, The pion: an enigma within the Standard Model, J. Phys. G. 43 (2016) 073001.

[4] R. J. Perry, A. Kızılersü, A. W. Thomas, An improved hadronic model for pion electroproduction, Phys. Lett. B 807 (2020) 135581. arXiv:2005.01395, doi:10.1016/j.physletb.2020.135581.

[5] T. K. Choi, K. J. Kong, B. G. Yu, Pion and proton form factors in the Regge description of electroproduction $p(e, e'\pi^+)n$, J. Korean Phys. Soc. 67 (7) (2015) 1089–1094. arXiv:1508.00969, doi:10.3938/jkps.67.1089.

[6] M. Vanderhaeghen, M. Guidal, J. M. Laget, Regge description of charged pseudoscalar meson electroproduction above the resonance region, Phys. Rev. C 57 (1998) 1454–1457. doi:10.1103/PhysRevC.57.1454.

[7] Z. Ahmed, et al., Dempgen: Physics event generator for deep exclusive meson production at jefferson lab and the eic, Computer Physics Communications 308 (2025) 109444. doi:https://doi.org/10.1016/j.cpc.2024.109444.
URL https://www.sciencedirect.com/science/article/pii/S0010465524003679

[8] A. Jentsch, et al., EIC MC afterburner.
URL https://github.com/eic/afterburner

[9] T. Kutz, Electron ID (2025).
URL https://github.com/eic/snippets/tree/main/ElectronID

[10] M.Arratia, S. Maple, B.Schmookler,R. Montgomery, S.J.D. Kay, G.M. Huber, The t_{RECO} Convention, unpublished, in progress ePIC technical note/convention. (2025).

[11] S.J.D. Kay, Generic calculation of t_{eXBABE} (2025).
URL https://github.com/eic/snippets/blob/main/Exclusive/teXBABE.h

[12] A. Airapetian, et al., Cross-sections for hard exclusive electroproduction of pi+ mesons on a hydrogen target, Phys. Lett. B 659 (2008) 486–492. arXiv:0707.0222, doi:10.1016/j.physletb.2007.11.079.

[13] F. Aaron, et al., Measurement of Leading Neutron Production in Deep-Inelastic Scattering at HERA, Eur. Phys. J. C 68 (2010) 381–399. arXiv:1001.0532, doi:10.1140/epjc/s10052-010-1369-4.

[14] T. Vrancx, J. Ryckebusch, Charged pion electroproduction above the resonance region, Phys. Rev. C 89 (2) (2014) 025203. arXiv:1310.7715, doi:10.1103/PhysRevC.89.025203.

[15] G. Huber, et al., Charged pion form-factor between $Q^2 = 0.60$ GeV^2 and 2.45 GeV^2. II. Determination of, and results for, the pion form-factor, Phys. Rev. C 78 (2008) 045203. arXiv:0809.3052, doi:10.1103/PhysRevC.78.045203.

[16] T. Horn, et al., Scaling study of the pion electroproduction cross sections and the pion form factor, Phys. Rev. C 78 (2008) 058201. arXiv:0707.1794, doi:10.1103/PhysRevC.78.058201.

[17] J. Volmer, et al., Measurement of the Charged Pion Electromagnetic Form-Factor, Phys. Rev. Lett. 86 (2001) 1713–1716. arXiv:nucl-ex/0010009, doi:10.1103/PhysRevLett.86.1713.

[18] T. Horn, et al., Determination of the Pion Charge Form Factor at $Q^2 = 1.60$ and 2.45 $(\mathrm{GeV}/c)^2$, Phys. Rev. Lett. 97 (2006) 192001. arXiv:nucl-ex/0607005, doi:10.1103/PhysRevLett.97.192001.

[19] V. Tadevosyan, et al., Determination of the pion charge form factor for Q^2 = 0.60–1.60 GeV^2, Phys. Rev. C 75 (2007) 055205. arXiv:nucl-ex/0607007, doi:10.1103/PhysRevC.75.055205.

[20] H. Blok, et al., Charged pion form factor between Q^2=0.60 and 2.45 GeV^2. I. Measurements of the cross section for the ^{1}H$(e, e'\pi^+)n$ reaction, Phys. Rev. C 78 (2008) 045202. arXiv:0809.3161, doi:10.1103/PhysRevC.78.045202.

[21] G. Huber, et al., Separated Response Function Ratios in Exclusive, Forward $\pi^\pm$ Electroproduction, Phys. Rev. Lett. 112 (18) (2014) 182501. arXiv:1404.3985, doi:10.1103/PhysRevLett.112.182501.

[22] G. Huber, et al., Separated Response Functions in Exclusive, Forward $\pi^\pm$ Electroproduction on Deuterium, Phys. Rev. C 91 (1) (2015) 015202. arXiv:1412.5140, doi:10.1103/PhysRevC.91.015202.

[23] G. M. Huber, D. Gaskell, T. Horn, et al., Measurement of the Charged Pion Form Factor to High Q^2 and Scaling Study of the L/T-Separated Pion Electroproduction Cross Section at 11 GeV, jefferson Lab 12 GeV Experiment E12-19-006.
URL https://www.jlab.org/exp_prog/proposals/19/E12-19-006.pdf

[24] A. Actor, J. Korner, I. Bender, Il Nuovo Cimento 24A (1974) 369.